Key Engineering Materials
ISSN: 1662-9795, Vol. 1050, pp 205-214
doi:10.4028/p-ddO89X

Submitted: 2026-01-19
Revised: 2026-03-04
Accepted: 2026-03-04
Online: 2026-04-16

Study on the Apparent Friction Coefficient Between a Deformable and a Rough Rigid Body under Large Sliding

Renan B. Wojciechowski[1,b], Marta C. Oliveira[1,a*] and Diogo M. Neto[1,c]

[1]CEMMPRE, ARISE, Department of Mechanical Engineering, University of Coimbra, Pinhal de Marrocos,3030-788 Coimbra, Portugal

[a]marta.oliveira@dem.uc.pt, [b]rbw@dem.uc.pt, [c] diogo.neto@dem.uc.pt

Keywords: Numerical Analysis, Contact Element, Periodic boundary conditions, Sinusoidal roughness

Abstract. The mechanical analysis of sliding frictional contact under small scales is important to improve the understanding about the influence of the contact conditions on the real contact area and, consequently, on the apparent coefficient of friction. This study uses the finite element method to model the contact between an elastoplastic body and a rigid surface with a unidirectional sinusoidal topography, including large sliding. A sensitivity analysis is presented, studying the influence of the initial average pressure, local coefficient of friction and asperity wavelength on the contact conditions. The ratio between total tangential and normal force (apparent friction coefficient) reaches a steady state after a sliding distance of five roughness wavelengths, except for lower values of average initial contact pressure. Increasing the initial average contact pressure leads to an increase of the steady state apparent friction coefficient, particularly for a surface with sharper asperities. This increasing tends to stagnate also with the increase of the local friction coefficient. Withing the cases studied, increasing the initial average contact pressure from 25% to 100% of the material yield stress, leads to an increase of up to 0.07 in the apparent coefficient of friction and of the real-to-apparent contact area ratio up to 30%.

Introduction

The contact mechanics has attracted increasing attention because friction and wear are responsible for ~23% of the global energy consumption [1]. Improvements in the understanding of contact phenomena can contribute to reducing this cost and mitigating environmental impacts. Thus, design modifications in engineering systems are required, which can be supported by robust modelling and analysis of the contact mechanics to support decision-making.

The mechanical analysis of sliding frictional contact under small scales is important to improve understanding about the influence of the contact conditions on the real contact area [2] and, consequently, on the apparent coefficient of friction. The finite element method (FEM) is commonly adopted to perform this type of study, since it enables parametric analysis considering parameters such as the surface roughness or the contact pressure, to evaluate quantities such as the real contact area or the residual stresses (e.g. Gao [3] and Alfredsson [4]). This enables the development of friction laws to describe the dependency of the apparent coefficient of friction on those parameters, which can be applied in simpler, equivalent macroscopic models.

The concept of representative contact element (RCE) was introduced within the FEM to allow modelling contact phenomena at different scales, including the details of rough surfaces. For example, Wriggers [5] employed a RCE to develop a frictional law for an elastomer in contact with rigid surface. Carvalho [6] proposed a multiscale rough contact algorithm that considers RCEs at different scales, to estimate the real contact area in contact without sliding. The RCE consists of a unit cell (e.g. parallelepiped) with periodic boundary condition (PBC), i.e., the opposite parallel faces present the same displacement for counterpart nodes.

When modelling two bodies in contact, if one has a much higher stiffness than the other, it can be considered rigid. This assumption is common is sheet metal forming or when studying elastomers, such as in pulley and conveyor belt system (see [5] or in the contact between the tire and the road (see e.g. [7]). Although it is arguable if this assumption is valid for metal-metal

forming contacts, since both bodies may plastically deform at the asperity scale, some works have also adopted this approach [8]. When modelling a real surface at sufficiently small scales, the asperities should be represented rather than assuming their macro-scale regular geometry (e.g. perfectly plane). One approach is to define the surface topography through measurements (e.g. stylus profilers). However, measurements artefacts make it difficult to obtain a surface geometry that is compatible with numerical models [9, 10]. Consequently, some authors prefer to use a surface that is stochastically generated with a selection of roughness parameters [11, 12, 13]. This approach also improves the study repeatability and facilitates parametric analysis. Another way of representing the roughness is to approximate the topography by a superposition of sinusoids ([3, 5]). This allows to accurately model the elastomers' visco-elastic effects without an impractically fine finite element mesh, following the approach proposed by Wriggers [5]. In addition, a Weierstrass function can be employed to calculate the real contact area of a fractal surface, which may provide a more realistic description of engineering topographies [3, 14].

The aforementioned asperities are responsible for the geometric component of the friction force during sliding (e.g. ploughing effect), while the remaining is due to the local contributions [15]. The apparent coefficient of friction (μ^*) was defined by Lafaye [16] as the ratio between this total friction force and the applied normal force. As reviewed and discussed by Blau [15], the ratio μ^* is a convenient and useful engineering metric, supporting the design of machines and buildings. Therefore, it has been used to characterize the slide resistance of 3D printed surfaces with bio inspired textures [17], general polymer friction [5, 16] and the cutting performance of a machining tool [18].

The objective of this work is to investigate the influence of the initial average pressure $\overline{p_i}$, local Coulomb coefficient of friction (μ) and asperity wavelength (λ) on the apparent friction coefficient, when a deformable body slide against a rigid rough surface. Therefore, a finite element model that employs a RCE to assume an effectively infinite interface is used to perform a sensitivity analysis at the microscale. The ratio between the real contact area (A_r) and the apparent contact area (A_a) is estimated based on the number of interface nodes in contact over its total. This is an indirect measure of the ratio, which assumes that the distance between the nodes remains approximately uniform during the simulation. The apparent friction coefficient μ^* is evaluated during sliding as the ratio between the total tangential and normal force components. Finally, the average contact pressure during the slide ($\overline{p}$) and shear stress and distortion are reported.

Finite Element Model

The contact between a rough rigid surface and a flat deformable body was modelled using an RCE, under plane strain conditions. Local interfacial friction was described using Coulomb's law with different constant values for the friction coefficient. The rough rigid surface was represented by a unidirectional sinusoidal surface. Considering the roughness average of a typical machined surface R_a=3.2 μm [19], the corresponding wave amplitude is g=5.03 μm. Two different values of the ratio between the amplitude and the wavelength (λ) were studied, namely g/λ=0.01 and g/λ=0.02, which lie within the range suggested by Gao [3]. Accordingly, the wavelengths considered are λ=502.65 μm and λ=251.33 μm. The roughness wavelengths defined at the microscale fall within the range admissible for which macroscale constitutive models remain applicable. The rigid surface is composed by at least six waves in order to allow large sliding distances between the RCE and the rigid surface. The geometry of the rigid sinusoidal surface was discretized with Nagata patches [20].

The RCE is presented in Fig. **1**. It has a parallelepiped geometry with a width equal to the wavelength λ and a height of 3λ, which ensures a uniform stress state at the upper surface, as suggested in [3]. The length along the out-of-plane direction is 8 μm. The RCE was discretized with hexahedral finite elements, using selective reduced integration, considering four zones with element sizes of $\lambda/40$, $\lambda/20$, $\lambda/10$ and $\lambda/5$. The non-conforming mesh is shown in Fig. **1** (c). Each zone has approximately the same height and they are connected through the hanging nodes feature [21]. The mechanical behaviour of the RCE is assumed isotropic and elastic-plastic, described by the von

Mises yield criterion. Accordingly, the Young's modulus is 210 GPa, the Poisson's ratio is 0.3 and the yield strength is 1.5 GPa. The plastic behaviour is described by the Swift law, such that the flow stress $Y= 1.505(\varepsilon_0+\varepsilon^p)^{0.001}$ (the small hardening coefficient is chosen to approximate an almost perfectly plastic behaviour).

The numerical simulation of the contact between the RCE and the rough rigid surface comprises two stages. First, the rigid surface is pressed against the RCE by imposing a vertical displacement until an initial average contact pressure $\bar{p}_i$ is reached, as shown in Fig. **1** (a). Four different values of $\bar{p}_i$ were adopted, which were defined according to the yield strength of the material, namely 25%, 50%, 75% and 100% of the yield strength. Then, large sliding is generated by imposing a sliding distance $\Delta s=5\lambda$ to the rigid surface, as shown in Fig. **1** (b). During this second stage, the nodes on the upper face of the RCE are clamped, since it is a boundary condition easy to impose. The periodic boundary conditions associated with the RCE allow the representation of an infinite contact interface and ensure continuity of displacement and stress fields across the lateral boundaries [6]. All numerical simulations were carried out using the in-house finite element code DD3IMP [22].

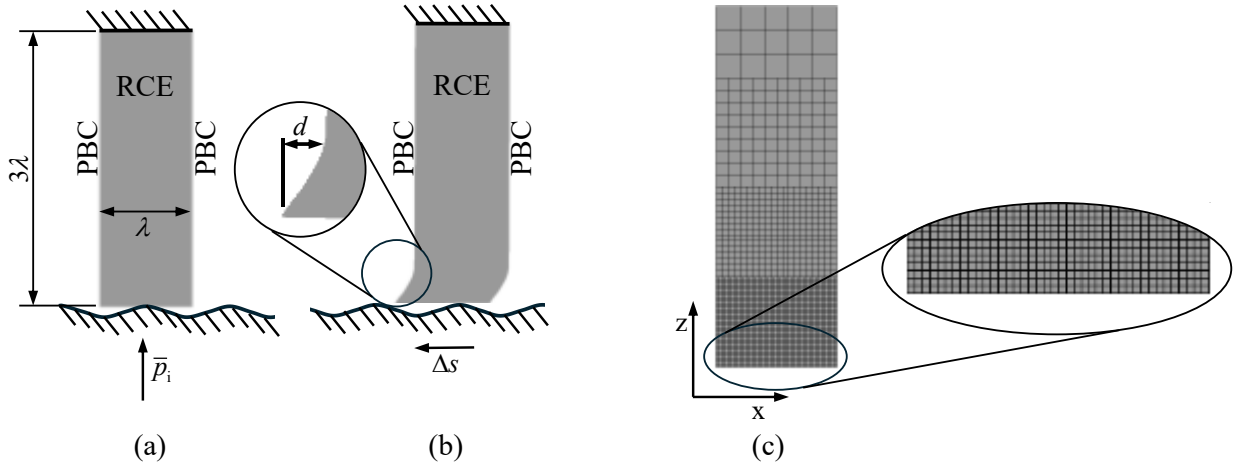

Fig. 1. Schematic of the contact between a rough rigid surface and deformable RCE: (a) rigid surface pressed against the RCE; (b) sliding of the rigid surface against the RCE; (c) non-conforming finite element mesh of the RCE.

Results and Discussion

Real Contact Area. The discretization of the contact surface (see Fig. **1** (c)), together with the use of a node-to-segment algorithm for handling contact, results in oscillations when the number of nodes in contact is used to evaluate the real contact area. Accordingly, the ratio A_r/A_a presented in this work must be interpreted as a discrete approximation, which must be improved in future works based on the contact variables [23]. The ratio A_r/A_a was evaluated during the pressing phase of a rigid surface against the RCE, leading to a step-like behaviour as shown in Fig. **2**. This figure shows the evolution of this ratio as the normal load increases, comparing two different values of g/λ, for μ=0.10 at the contact interface. The real contact area increases approximately linearly with the applied normal load (R^2=0.98), which is consistent with elastic–plastic asperity deformation. The slope is higher for the lower ratio g/λ because it is more comparable to a flat surface, which would present A_r/A_a=1. In classical rough-surface contact models, only a small fraction of the apparent area actually carries load, even under high contact pressures [24]. It has been shown that for an elastoplastic rough surface there is a linear load-area relation at small contact fraction (A_r/A_a ~0.45), and the proportionality is determined by the mechanical properties and surface morphology. As the contact fraction increases further, dramatically higher load will be required owing to asperity interactions [25]. One can expect that the contact area fraction calculated in this study to be higher than the one obtained with 3D models due to the plane strain conditions, i.e. the real contact area is composed by stripes instead of islands.

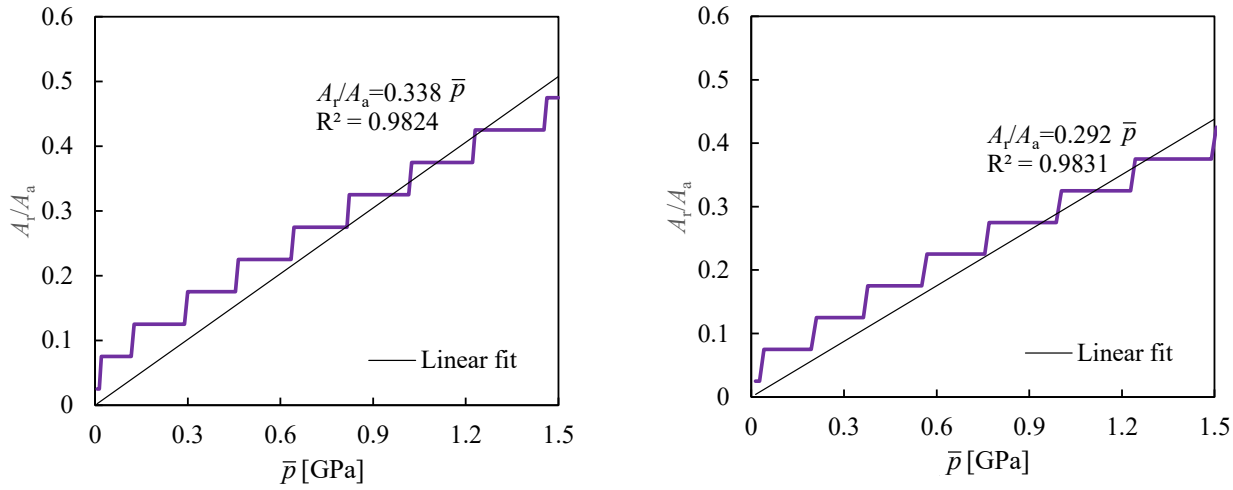

Fig. 2. Evolution of the ratio between the real contact area (A_r) and the apparent contact area (A_a) during the pressing of a rigid surface against the RCE considering μ=0.10 at the interface for: (a) g/λ=0.01; (b) g/λ=0.02.

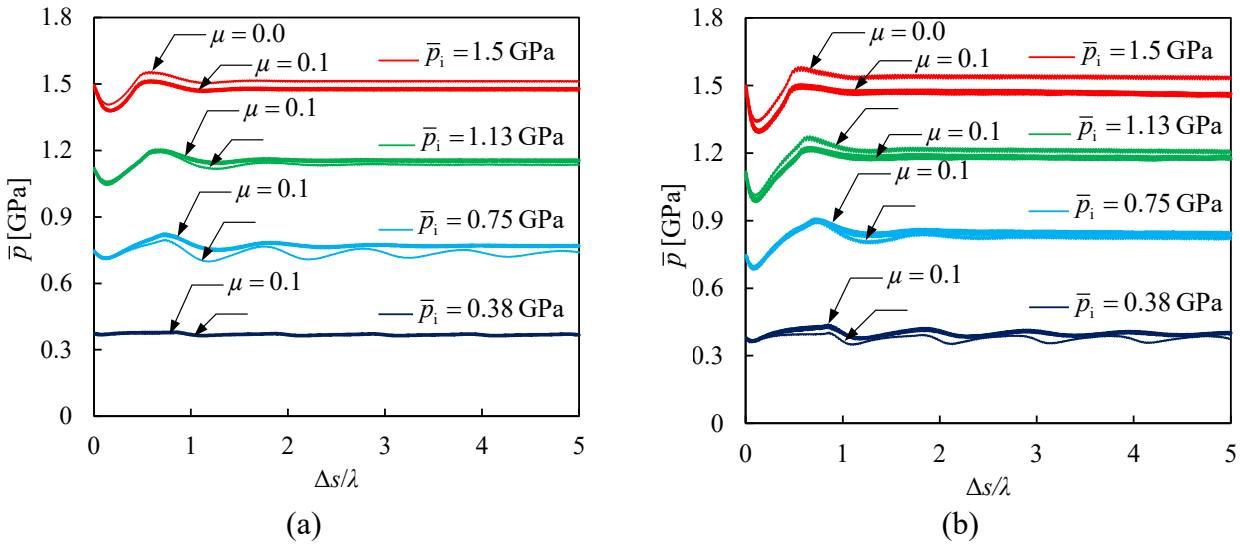

Fig. 3. Evolution of the average contact pressure during the sliding of a rigid surface against the RCE for different levels of initial average contact pressure: (a) g/λ=0.01; (b) g/λ=0.02.

During the sliding phase of the rigid surface against the RCE, its position normal to the surface is kept constant (see Fig. **1** (b)). Fig. 3 shows the evolution of the average contact pressure during sliding, comparing different values of $\bar{p}_i$ and two levels of friction coefficient. The horizontal axis represents the normalized sliding distance ($\Delta s/\lambda$), indicating that the total applied sliding corresponds to five wavelengths of the rigid surface roughness.

As sliding stage begins, the average contact pressure decreases due to the development of a shear stress component, particularly for high values of the initial average contact pressure. Around $\Delta s/\lambda$=0.15, the average contact pressure starts to increase because of the misalignment between the asperity peaks and the deformable surface valleys created during the compression phase. When these points begin to realign, the pressure decreases again. This cyclic behaviour repeats, with progressively lower amplitude. In most cases, the average contact pressure can be considered stable after sliding over approximately two wavelengths of the rigid surface roughness. The effect of the friction coefficient μ on the predicted average contact pressure is low, as shown in Fig. 3. For $\bar{p}_i$=1.5 GPa, the increase of the friction coefficient leads to a decrease of the predicted average contact pressure, particularly for g/λ=0.02. On the other hand, for $\bar{p}_i$=0.38 GPa and g/λ=0.02, the increase of the friction coefficient leads to a slight increase of the predicted average contact

pressure. Although sliding is imposed under fixed normal displacement, rather than fixed normal load, which is more commonly adopted in this type of studies, the results show that this condition also leads to stable average contact pressure.

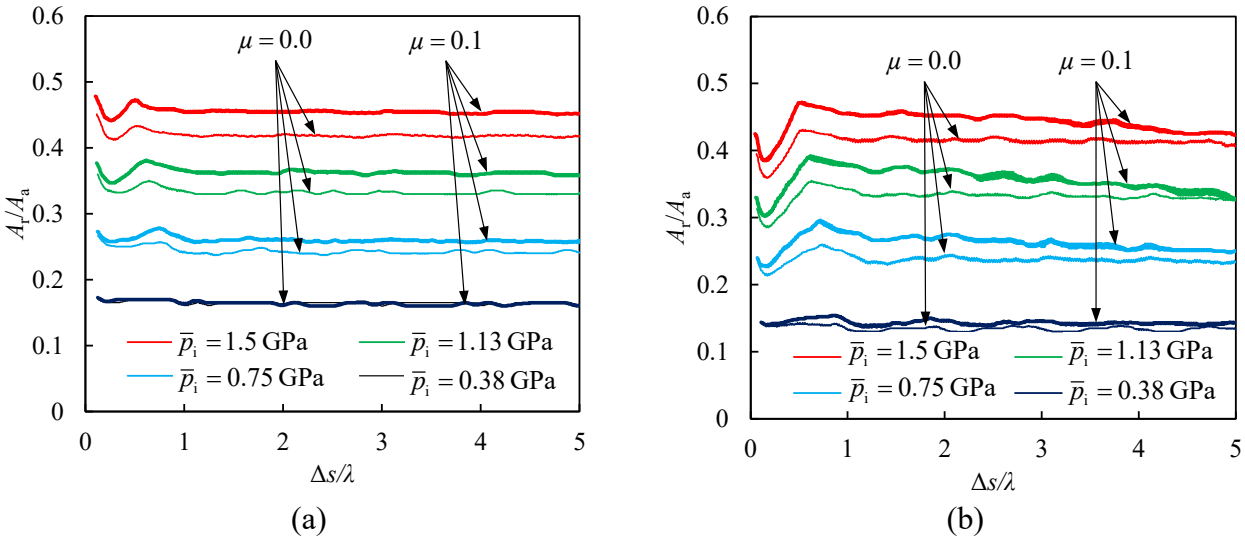

Fig. 4. Evolution of the ratio between the real contact area (A_r) and the apparent contact area (A_a) during the sliding of a rigid surface against the RCE, considering different values of initial average contact pressure and coefficient of friction: (a) g/λ=0.01; (b) g/λ=0.02.

Due to the use of the number of contact nodes to calculate the real contact area, during sliding sudden jumps can occur. Therefore, a moving average was applied to smooth the data during the sliding stage. Fig. 4 presents the evolution of the ratio between the real and apparent contact area during the sliding stage. Under frictionless conditions (μ=0.0), the steady state is achieved for $\Delta s/\lambda$<5, except for $\bar{p}_i$=0.38 GPa. However, when friction is considered (μ=0.1), a steady state is achieved only for g/λ=0.01, as shown in Fig. 4 (a). In contrast, for g/λ=0.02, the real contact area exhibits a slight (continuous) decrease throughout the sliding process, as illustrated in Fig. 4 (b). The increase of the friction coefficient leads to a global increase of the real contact area, particularly for high levels of initial average contact pressure. Considering $\bar{p}_i$=1.5 GPa and g/λ=0.01, the ratio A_r/A_a increases about 2.5% as μ increases from 0.0 to 0.1.

Apparent Friction Coefficient. The apparent friction coefficient μ^* was evaluated as the ratio between the tangential and normal force components during the sliding phase. Fig. 5 shows the evolution of μ^* during the sliding phase, comparing four values of initial average contact pressure and three different values of μ. Globally, increasing μ leads to an increase of μ^*. Moreover, the apparent friction coefficient increases when the ratio g/λ increases from 0.01 to 0.02, as shown by comparing Fig. 5(a) with Fig. 5(b). This occurs due the higher slope between the valleys and the peaks for g/λ 0.02, resulting in sharper asperities that penetrates the RCE and increases sliding resistance. Hence, increasing the initial average contact pressure also increases the apparent friction coefficient. One can expect that the apparent friction coefficient μ^* calculated in this study to be higher than the one obtained with 3D models due to the plane strain conditions.

The Coulomb friction law states that the ratio between the tangential and normal force is always constant. However, this relation was not observed in the numerical results due to the roughness present at the interface of RCE. As shown in Fig. 5, for most cases μ^* attains a steady state value. Therefore, the values of μ^* attained for $\Delta s/\lambda$=5 were extracted, for all cases, and assumed as the ones corresponding to the apparent friction coefficient at the steady state regime (μ^*_{ss}), since the variation beyond Δs/λ>4 is at most 0.006. Fig. 6 presents μ^*_{ss} considering different values of input friction coefficient μ and four levels of initial average contact pressure. Increasing the initial average contact pressure leads to an increase of μ^*_{ss}, particularly for g/λ=0.02. The interlocking of asperities is generated when the initially flat deformable body acquires roughness when pressed against a rough rigid surface. This effect is amplified by the pressure $\bar{p}_i$. When the average contact

pressure is low ($\bar{p}_i$<0.38 GPa), the μ^*_{ss} is approximately the input μ, particularly for g/λ=0.01. On the other hand, increasing both the μ and the $\bar{p}_i$, the obtained μ^*_{ss} present a stagnation in their increase.

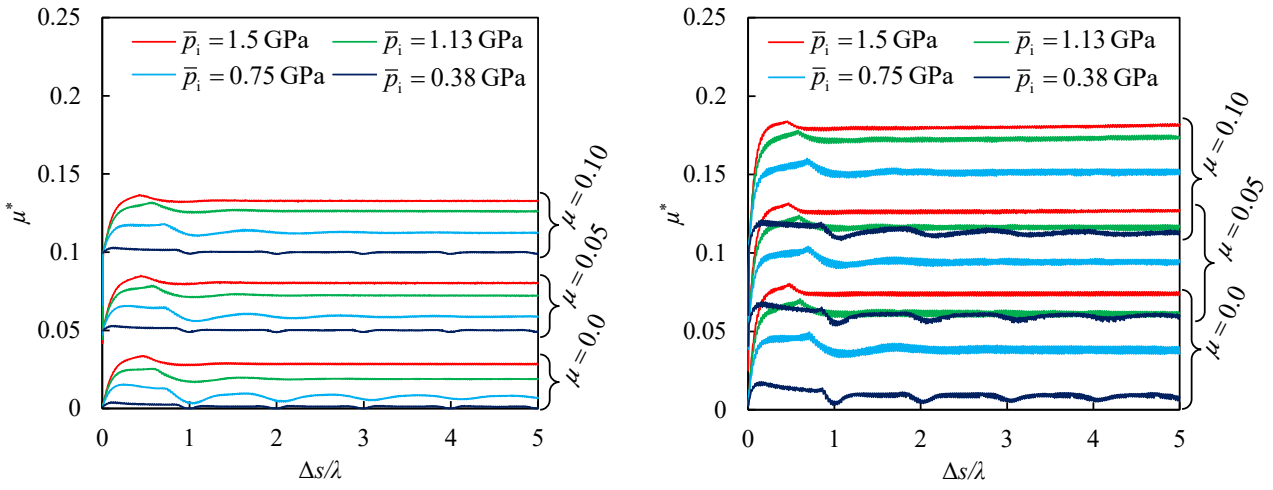

Fig. 5. Evolution of the apparent friction coefficient during the sliding of a rigid surface against the RCE for different levels of initial average contact pressure: (a) g/λ=0.01; (b) g/λ=0.02.

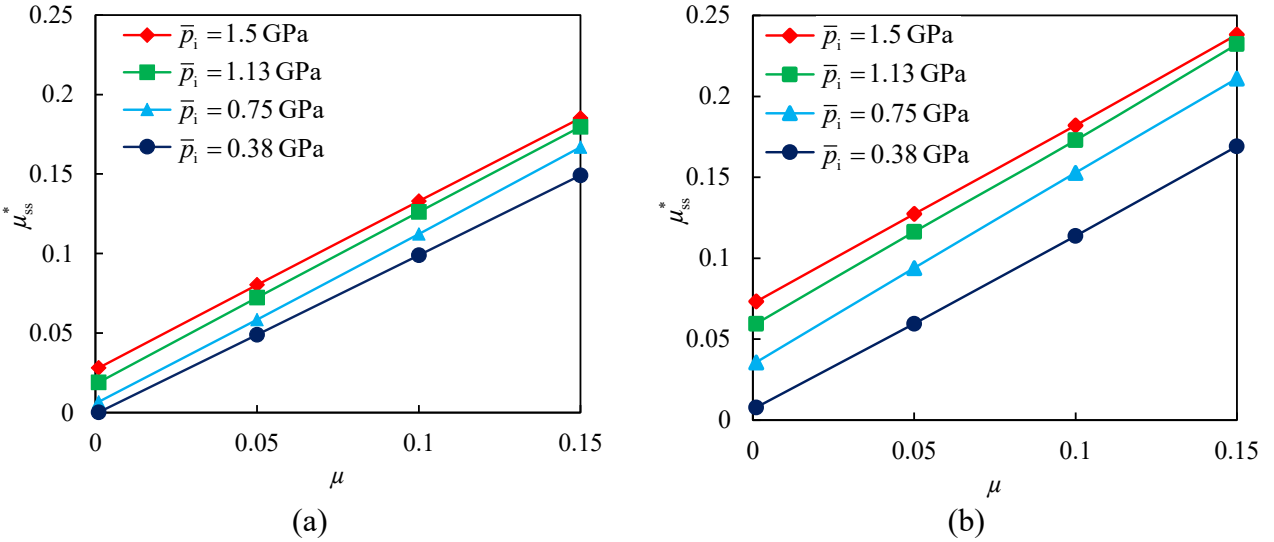

Fig. 6 Apparent friction coefficient evaluated at the steady state as a function of the input friction coefficient, considering different levels of initial average contact pressure: (a) g/λ=0.01; (b) g/λ=0.02.

Strain and Stress Distribution. The plastic strain distribution at $\Delta s/\lambda$<5 was evaluated along the mid-width of the RCE, as show in the detail of Fig. 7 (b). Fig. 7 compares the plastic strain distributions for different levels of initial average contact pressure and two different values of μ. The maximum value occurs near the contact surface and decreases as the distance to the surface increases. Increasing the ratio g/λ leads to an increase of the maximum plastic strain value and reduces the height of the region with plastic deformation. Increasing the initial contact pressure also leads to an increase of the plastic strain due to the increase of the level of stress at the interface generated by the increase of compression force. In the same way, the increase the friction coefficient leads to an increase of the plastic strain, particularly for the ratio g/λ=0.01. Additionally, the increase of μ also moves the maximum plastic strain closer to the surface, as shown in Fig. 7. This agrees with the Hertz solution, where the maximum stress moves from the subsurface to the surface when μ increases.

It must be noted that even relatively moderate normal load leads to extremely high local deformations: accumulated plastic strain reaches 300%. Normal metal materials are not supposed to bear such high deformations. Consequently, a damage or/and a fracture model should be incorporated in the analysis to get more physical results [26]. Nevertheless, the plastic strain levels are strongly dependent on the hardening law. Although not shown here, a small increase of the hardening coefficient drastically reduces the maximum values attained.

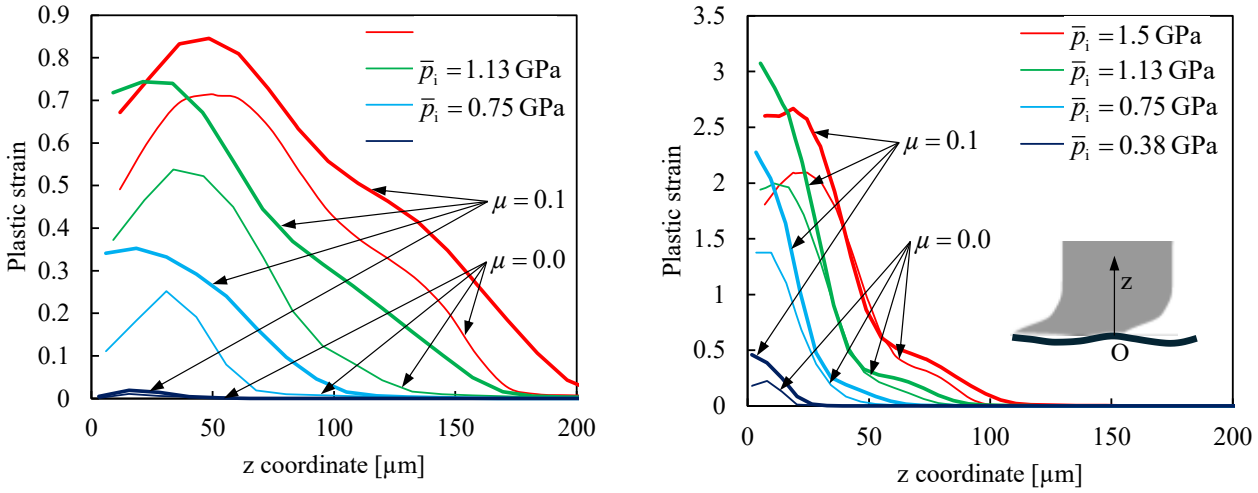

(a) (b)

Fig. 7. Plastic deformation distribution at the mid-width of the RCE after sliding against a rigid surface for different levels of initial average contact pressure: (a) g/λ=0.01; (b) g/λ=0.02.

The sliding of the rigid surface from the right side to the left side induces a shear deformation on the deformable body. This effect was quantified by the total tangential displacement, d, of the left lower node. Fig. 8 presents the evolution of this distance during the sliding stage, highlighting the global increase of d. The distortion of the deformable body is higher for g/λ=0.02, as shown in Fig. 8 (b). Increasing either the initial contact pressure or the friction coefficient yields an increase of the distortion. For cases that achieve a steady state apparent friction coefficient (see Fig. 5), the distance d is continuously increasing during the sliding stage. The fluctuations are consequence of the asperity entering in contact with the monitored node, which produces an increase of the local tangential loading.

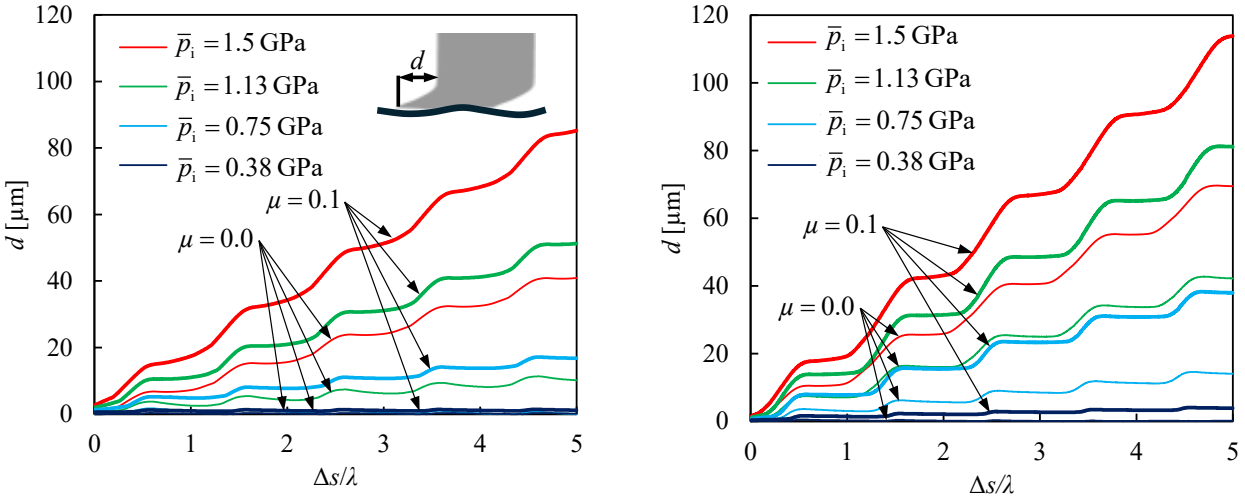

(a) (b)

Fig. 8. Evolution of the tangential displacement of node located at the left lower corner of the RCE while sliding against a rigid surface for different levels of initial average contact pressure: (a) g/λ=0.01; (b) g/λ=0.02.

Fig. **9** presents the distribution of the shear stress (τ_{xy}) evaluated at the RCE after sliding against the rigid rough surface, considering different conditions for g/λ=0.01. The shear stress distribution is approximately symmetric in relation to the mid-width plane, when the initial average contact pressure is $\bar{p}_i$=0.75 GPa and the friction coefficient is zero (see Fig. **9** (a)). This distribution is like the one obtained in the Hertz contact theory, because the contact occurs locally in a small area. Increasing the initial average contact pressure leads to the distortion of the deformable body due to the sliding and, consequently, of the shear stress distribution, as shown in Fig. **9** (b). Using the same value of pressure, the increase of the friction coefficient amplifies the geometrical distortion, as shown in Fig. **9** (c).

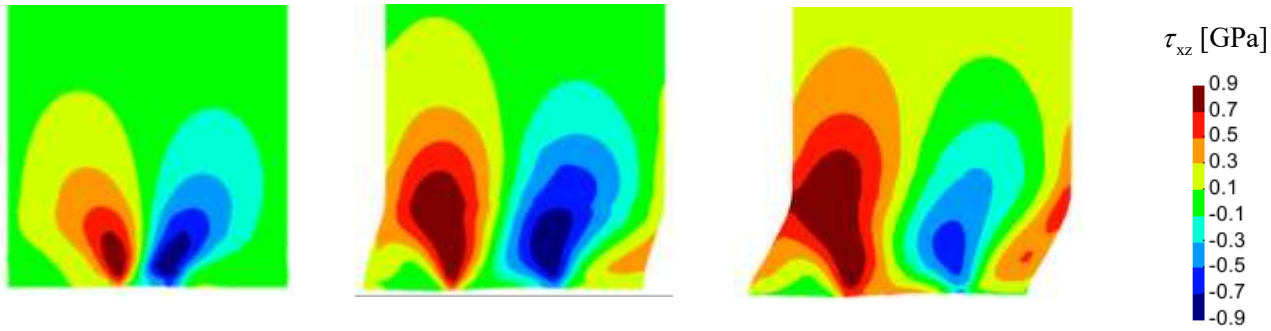

(a) (b) (c)

Fig. 9. Shear stress distribution on the RCE after sliding against the rigid surface with g/λ=0.01: (a) μ=0.0 and $\bar{p}_i$=0.75 GPa; (b) μ=0.0 and $\bar{p}_i$=1.5 GPa; (c) μ=0.1 and $\bar{p}_i$=1.5 GPa.

Conclusions

This paper presented a numerical investigation of the frictional contact conditions arising from surface roughness in the interaction between a deformable body and a rough rigid surface under large sliding. The finite element method was employed to simulate the contact problem, making use of a representative contact element (RCE) and plane strain conditions to reduce the computational cost. The influence of the local friction coefficient, the initial average contact pressure and roughness wavelength was analysed, with particular emphasis on the steady-state sliding regime.

Since sliding is imposed under a fixed normal displacement, the average contact pressure remains approximately constant throughout the sliding stage. The results show that the main parameter governing the real contact area is the initial average contact pressure, whereas both the friction coefficient and the roughness ratio g/λ have only a minor influence on this quantity. In contrast, the apparent friction coefficient is significantly affected by all three parameters, increasing with higher local friction coefficient, higher initial average contact pressure, and larger values of g/λ. For a surface roughness ratio of g/λ=0.02 and a local friction coefficient of μ=0.05, the predicted apparent friction coefficient is approximately μ^*=0.09, when the initial average contact pressure is about half of the material yield stress.

Although the applied initial average contact pressure is at most equal to the yield stress of the material, the roughness of the rigid contact surface induces high levels of plastic deformation in the vicinity of the contact interface. Indeed, for a surface roughness ratio of g/λ=0.01, the maximum equivalent plastic strain exceeds 50% when the initial average contact pressure is larger than 75% of the yield stress. The high shear stress levels at the contact interface induce significant distortion of the RCE in the vicinity of the contact zone. This effect is amplified for higher local friction coefficients, higher initial average contact pressures, and larger values of the roughness ratio g/λ. In this exploratory work, an almost perfectly plastic behaviour was assumed, to simplify the analysis. This enabled the validation of the contact area fraction under loading, but disabled further comparisons for the sliding stage.

Acknowledgements

This research is sponsored by national funds through FCT – Fundação para a Ciência e a Tecnologia, under projects UID/00285/2025 and LA/P/0112/2020. It was also supported by the project Sim2Adapt (ref. 2022.08459.PTDC). All the supports are gratefully acknowledged.

References

[1] K. Holmberg, A. Erdemir, Influence of tribology on global energy consumption, costs and emissions, Friction, vol. 5, no. 3, pp. 263–284, Sep. 2017, doi: 10.1007/s40544-017-0183-5.

[2] B. N. J. Persson, Theory of rubber friction and contact mechanics, The Journal of Chemical Physics, vol. 115, no. 8, pp. 3840–3861, Aug. 2001, doi: 10.1063/1.1388626.

[3] Y. F. Gao, A. F. Bower, K.-S. Kim, L. Lev, Y. T. Cheng, The behavior of an elastic–perfectly plastic sinusoidal surface under contact loading, Wear, vol. 261, no. 2, pp. 145–154, Jul. 2006, doi: 10.1016/j.wear.2005.09.016.

[4] Alfredsson and Olsson, Standing contact fatigue testing of a ductile material: surface and subsurface cracks, Fatigue Fract Eng Mat Struct, vol. 23, no. 3, pp. 229–240, Mar. 2000, doi: 10.1046/j.1460-2695.2000.00269.x.

[5] P. Wriggers, J. Reinelt, Multi-scale approach for frictional contact of elastomers on rough rigid surfaces, Computer Methods in Applied Mechanics and Engineering, vol. 198, no. 21–26, pp. 1996–2008, May 2009, doi: 10.1016/j.cma.2008.12.021.

[6] R. P. Carvalho, Multi-scale Modelling of Contact Interfaces, Universidade do Porto, Porto, Portugal, 2021.

[7] M. Klüppel, G. Heinrich, Rubber Friction on Self-Affine Road Tracks, Rubber Chemistry and Technology, vol. 73, no. 4, pp. 578–606, Sep. 2000, doi: 10.5254/1.3547607.

[8] J. Hol, Multi-scale friction modeling for sheet metal forming, University of Twente, 2013. doi: 10.3990/1.9789077172988.

[9] Francesc Pérez-Ràfols, Andreas Almqvist, Generating randomly rough surfaces with given height probability distribution and power spectrum, Tribology International, vol. 131, pp. 591–604, Mar. 2019, doi: 10.1016/j.triboint.2018.11.020.

[10] Y. Wang, Y. Liu, Preparation of measured engineering surfaces for modeling tribological systems, part I: Characterization and reconstruction, Tribology International, vol. 199, p. 110026, Nov. 2024, doi: 10.1016/j.triboint.2024.110026.

[11] S. Zhang, C. Zhang, A New Deterministic Model for Mixed Lubricated Point Contact With High Accuracy, Journal of Tribology, vol. 143, no. 10, p. 102201, Oct. 2021, doi: 10.1115/1.4049328.

[12] F. Pérez-Ràfols, A. Almqvist, On the stiffness of surfaces with non-Gaussian height distribution, Sci Rep, vol. 11, no. 1, p. 1863, Jan. 2021, doi: 10.1038/s41598-021-81259-8.

[13] Y. Waddad, V. Magnier, P. Dufrénoy, G. De Saxcé, A multiscale method for frictionless contact mechanics of rough surfaces, Tribology International, vol. 96, pp. 109–121, Apr. 2016, doi: 10.1016/j.triboint.2015.12.023.

[14] M. Ciavarella, G. Demelio, J. R. Barber, Y. H. Jang, Linear elastic contact of the Weierstrass profile, Proc. R. Soc. Lond. A, vol. 456, no. 1994, pp. 387–405, Feb. 2000, doi: 10.1098/rspa.2000.0522.

[15] P. J. Blau, The significance and use of the friction coefficient, Tribology International, vol. 34, no. 9, pp. 585–591, Sep. 2001, doi: 10.1016/S0301-679X(01)00050-0.

[16] S. Lafaye, C. Gauthier, R. Schirrer, Analysis of the apparent friction of polymeric surfaces, J Mater Sci, vol. 41, no. 19, pp. 6441–6452, Oct. 2006, doi: 10.1007/s10853-006-0710-7.

[17] S. Mzali, F. Elwasli, S. Mezlini, K. Hajlaoui, N. H. Alrasheedi, Tribological behavior of 3D printed biomimetic surfaces, Tribology International, vol. 193, p. 109352, May 2024, doi: 10.1016/j.triboint.2024.109352.

[18] N. Chen et al., Improving cutting performance of nickel-based alloy by graphene modified diamond tools, CIRP Annals, vol. 74, no. 1, pp. 145–149, 2025, doi: 10.1016/j.cirp.2025.04.034.

[19] O. Çolak, C. Kurbanoğlu, M. C. Kayacan, Milling surface roughness prediction using evolutionary programming methods, Materials & Design, vol. 28, no. 2, pp. 657–666, Jan. 2007, doi: 10.1016/j.matdes.2005.07.004.

[20] T. Nagata, Simple local interpolation of surfaces using normal vectors, Computer Aided Geometric Design, vol. 22, no. 4, pp. 327–347, May 2005, doi: 10.1016/j.cagd.2005.01.004.

[21] T. Fries, A. Byfut, A. Alizada, K. W. Cheng, A. Schröder, Hanging nodes and XFEM, Numerical Meth Engineering, vol. 86, no. 4–5, pp. 404–430, Apr. 2011, doi: 10.1002/nme.3024.

[22] L. F. M. Menezes, Modelação tridimensional e simulação numérica dos processos de enformação por deformação plástica: aplicação à estampagem de chapas metálicas, PhD Thesis, Universidade de Coimbra, 1995.

[23] M. C. Oliveira, J. L. Alves, and L. F. Menezes, Algorithms and Strategies for Treatment of Large Deformation Frictional Contact in the Numerical Simulation of Deep Drawing Process, Arch Computat Methods Eng, vol. 15, no. 2, pp. 113–162, Jun. 2008, doi: 10.1007/s11831-008-9018-x.

[24] V. A. Yastrebov, G. Anciaux, J.-F. Molinari, On the accurate computation of the true contact-area in mechanical contact of random rough surfaces, Tribology International, vol. 114, pp. 161–171, Oct. 2017, doi: 10.1016/j.triboint.2017.04.023.

[25] W. Peng and B. Bhushan, sliding contact analysis of layered elastic/plastic solids with rough surfaces, Journal of Tribology, vol. 124, no. 1, pp. 46–61, Jan. 2002, doi: 10.1115/1.1401018.

[26] V. A. Yastrebov, J. Durand, H. Proudhon, and G. Cailletaud, Rough surface contact analysis by means of the Finite Element Method and of a new reduced model, Comptes Rendus. Mécanique, vol. 339, no. 7–8, pp. 473–490, Jun. 2011, doi: 10.1016/j.crme.2011.05.006.